ELSEVIER

Journal of Nuclear Materials 265 (1999) 44–59

journal of nuclear materials

A unified model of Zircaloy BWR corrosion and hydriding mechanisms

Peter Rudling [a,1], Gunnar Wikmark [b,1,*]

[a] *Vattenfall Bränsle, Vällingby, Sweden*
[b] *Materials Development, ABB Atom, SE-721 63 Västerås, Sweden*

Received 2 July 1998; accepted 25 September 1998

Abstract

A model explaining the uniform and nodular corrosion and hydriding behaviour in BWRs is presented. As illustration, three materials with different second phase particle (SPP) distributions have been characterised in the un-irradiated and irradiated conditions. One of the materials shows accelerated uniform corrosion at higher burn-ups, despite a similar alloy composition for all three materials. It is concluded that the SPP distribution and chemical composition is controlling the corrosion and hydriding behaviour at all stages, except in the pre-transition stage. It is further concluded that, of several simultaneous corrosion processes, one is normally rate limiting at each stage of corrosion development, but different corrosion processes are rate limiting at each stage.

1. Introduction

Corrosion and hydriding performance of zirconium fuel components in LWRs may today limit the maximum fuel discharge burn-up, which urges the development of new materials. Out-of-pile autoclave corrosion tests have been developed over the years to predict in-pile corrosion performance of zirconium alloys. However, these autoclave tests may normally at best predict corrosion behaviour of specific zirconium alloys within a limited chemical composition interval as well as of a narrow variation in manufacturing. Outside these ranges of conditions, the autoclave tests do neither predict the in-pile corrosion behaviour of the zirconium alloys nor rank the different alloys correctly. This fact indicates that the rate limiting step in the in-pile corrosion process of most zirconium alloys is different from that in the autoclave tests. Hence the autoclave tests will not be adequate in predicting the in-pile corrosion performance of most zirconium alloys.

To solve this problem, investigators have attempted to develop theories on zirconium alloy corrosion and hydriding processes for over 30 years. The theories found in the literature do generally at best explain only a small part of all the reported observations of corrosion and hydriding behaviour in-pile and out-of-pile of the various zirconium alloys being manufactured to date. In this communication we present a corrosion model that may explain the BWR corrosion and hydriding performance of Zircaloys in a general manner, based upon the material microstructure.

Section 2 describes the different materials, chemistry and manufacturing process used as examples in the presentation of this model. Section 3 presents the out-of-pile and in-pile corrosion and hydriding data, as well as results from characterisation of the microstructure of the studied materials. Section 5 presents the unified model based upon the results presented in Sections 2 and 3, as well as the discussion in Section 4.

* Corresponding author.
[1] Present address: Advanced Nuclear Technology, Uppsala Science Park, SE-751 83 Uppsala, Sweden. Tel.: +46-18 50 66 80; fax: +46-18 50 66 85; e-mail: ant@ant.se

0022-3115/99/$ – see front matter
PII: S0022-3115(98)00613-8

2. Materials and experimental methods

2.1. Materials

The ingot chemical composition and the heat treatments during manufacturing, here given as the cumulative annealing parameter A, of the different materials used as examples in this presentation are provided in Table 1. The cumulative heat treatment of the material is here described by the normalised annealing parmeter A, defined as

$$A = \Sigma t_i \exp\left(\frac{-Q}{RT_i}\right), \quad (1)$$

where i corresponds to the i th heat treatment (after the last β-quench operation) of the material at the temperature T_i (K) during the time t_i (h), R is the gas constant and Q an activation energy of 63 000 cal/mol [1].

2.2. SEM and TEM

The size distribution of the second phase particles, SPPs, of the materials were analysed in a scanning electron microscope, SEM, Jeol Model JSM 6400. The instrument was equipped with a high-performance backscattered electron detector, BSE, Link Tetra model. The SPP images were duplicated from Polaroid photographs to a transparent plastic film prior to quantification by an image analyser, IBAS 2000. The image analyser computer program for measuring the diameter of equivalent circles was used to assess the SPP size distribution.

An analytical electron microscope, ATEM (VG HB501) equipped with a field emission gun was used to determine the SPP sizes of the smallest SPPs as well as for analysing the SPP chemical composition as given in Table 3. About 40 SPPs were analysed for each material.

Two different specimen preparation techniques were utilised as follows:

- SPPs smaller than 25 nm were determined in ATEM. Thin foils were prepared by using the jet electropolishing technique. Disk specimens, 3 mm in diameter, were mechanically polished to 0.05 mm and finally thinned by electropolishing at a voltage of 20 V in a mixture of 10% perchloric acid and 90% ethanol at −30°C.
- For SPPs larger than 30–50 nm the SEM instrument was used. After careful mechanical grinding with 0.25 μm diamond paste, and a very short, 5 s, final electrochemical polishing as described above, the specimen surface condition was sufficiently smooth to allow differentiation between the SPPs and the matrix. This was done by pure Z-contrast by working in the BSE mode, generally with 20 kV acceleration voltage.
- The number of fields investigated was always more than 10 and the number of particles for each material more than 100 (ATEM) or 400 (ASEM), in order to have an adequate statistical number of particles for the distribution plots.

3. Results

3.1. In-pile results

The materials A, B, and C were irradiated in a Swedish BWR as fuel cladding tubes. At the outage the oxide thickness was measured by a non-destructive eddy-current equipment at 14 different axial rod elevations. The average value of the fourteen different rod oxide thickness values are plotted versus the assembly average burn-up in Fig. 1. It is clear that material C shows initially the highest corrosion rate followed by material B, while material A has the lowest initial corrosion rate. At higher burn-ups material A experiences a corrosion acceleration while the corrosion rate of the other materials levels off. The cladding tubes were also repeatedly visually inspected and the results showed that after one cycle of irradiation, the nodule frequency was largest on material C but also high for material B. No nodules were seen on material A. Inspections after subsequent cycles revealed that the nodules on materials B and C coalesced although the number of nodules formed apparently did not increase yet eventually the whole rod surface was covered by nodular oxide. Nodule formation was almost absent on material A during the first cycles of irradiation but eventually a few were detected at high burn-ups. The corrosion acceleration observed late in-life of material A, as shown in Fig. 1 is hence not related to nodule formation but to an acceleration of the uniform corrosion type.

Table 1
Ingot chemical composition and A parameter of the studied materials

Material	Chemical composition					log A [a]
	Sn (wt%)	Fe (wt%)	Cr (wt%)	Ni (wt%)	Si (ppm)	
A	1.43–1.51	0.10–0.11	0.07–0.10	0.05	<20	−16.0
B	1.43–1.51	0.10–0.11	0.07–0.10	0.05	<20	−14.2
C	1.46–1.54	0.11–0.13	0.11–0.12	0.05–0.06	<20	−13.9

[a] Calculated on heat treatments after the last β quenching according to the expression in the text.

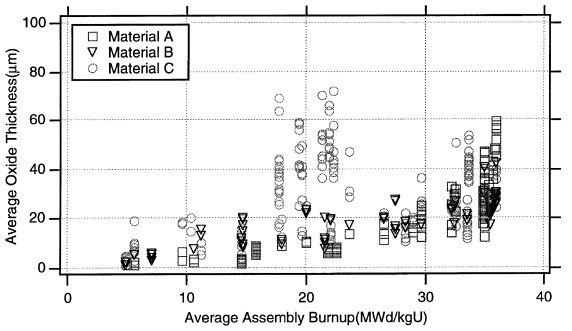

Fig. 1. Corrosion data for materials *A*, *B*, and *C* obtained in-pile.

3.2. Characterisation of material microstructure

3.2.1. Characterisation of matrix in Zircaloy material

The iron, chromium and nickel matrix contents in the un-irradiated materials *A* and *C* were characterised by atom probe analysis. The equipment and method used are described elsewhere [2]. A total of 34 000 and 48 000 ions, respectively, were used to determine the composition of the materials. For material *C* 36 ± 26 ppm (by weight) iron, 17 ± 17 ppm chromium, and 19 ± 19 ppm nickel were determined. Similar results were obtained for material *A* with 38 ± 22 ppm iron and 24 ± 17 ppm chromium. These results show that the matrix in both Zircaloy-2 materials is markedly depleted of the alloying elements iron, chromium and nickel. The total content of the sum of the iron, chromium and nickel was 72 and 62 ppm for materials *C* and *A*, respectively, while a total of 2500 to 2900 ppm, respectively, of the sum of iron, chromium and nickel was added to the materials as alloying elements. Material *A* had a much lower accumulated annealing parameter, see Table 1, and it could be presumed that the matrix in this material would be supersaturated with iron, chromium and nickel. This does not seem to be the case based on the results presented here. Thus, the difference in the matrix iron, nickel, and chromium contents between material *A* and *C* is not significant. It is thus inferred that the difference in corrosion performance between materials *A* and *C*, Fig. 1, is not related to an initial difference in the iron, nickel and chromium matrix contents. The observation that a significant difference in log *A* parameter does not result in a significant difference in matrix composition corroborates with the results published by Wadman et al. [2].

3.2.2. Characterisation of SPPs in Zircaloy materials

The major fraction of the alloying elements are instead found as second phase particles, SPPs. Most of the manufacturing steps, and especially heat treatments, will affect the size distribution and the total number of SPPs found in the material [3,4].

It has also been reported previously [5–13] that irradiation will affect the size, structure, and chemical composition of second phase particles.

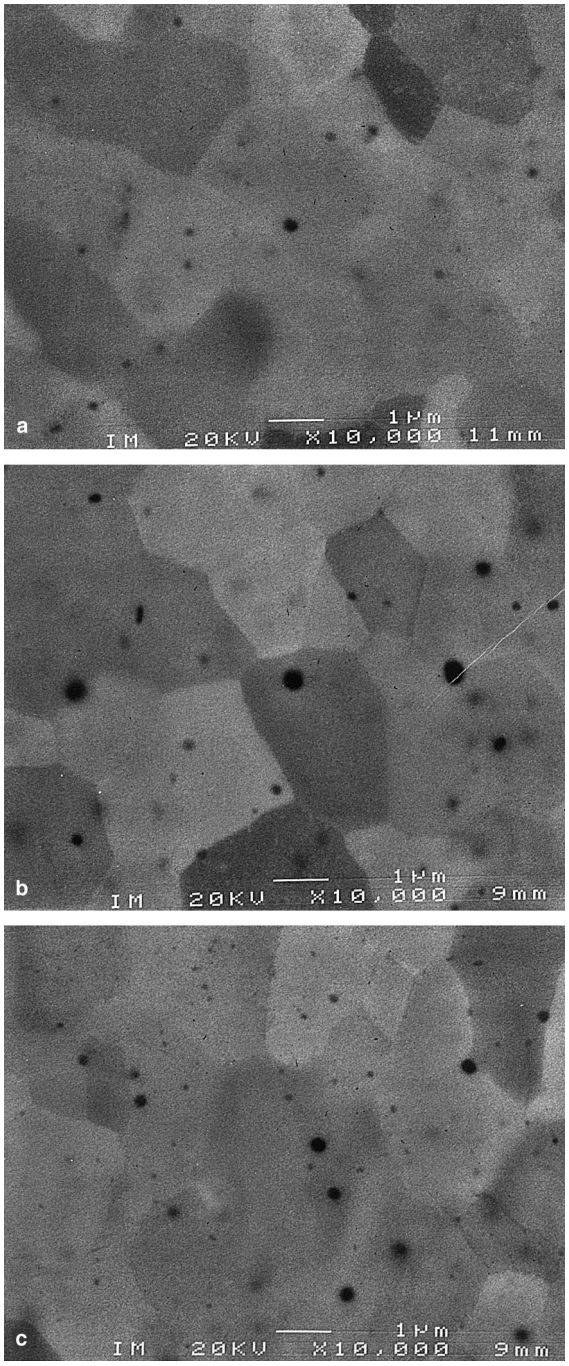

Fig. 2. Typical micro-graphs of the different materials, (a) material *A*, (b) material *B*, (*c*) material *C*, all 10 000× magnification in ASEM in BSE mode.

Table 2
Summary of SPP size distributions

Material	Instrument (magnif.)	No. of fields covered	No. of SPPs measured	Mean SPP size (nm)	SPP density (per mm^2)	SPP area fraction (%)
A	ATEM (200 kx)	14	136	29	3.8×10^6	3.8
A	SEM (10 kx)	64	615	92	4.0×10^5	0.30
B	SEM (10 kx)	40	670	83	7.0×10^5	0.47
C	SEM (10 kx)	48	406	164	3.5×10^5	0.96

3.2.2.1. Microstructure and SPP distribution of non-irradiated materials. Typical micro-graphs of the studied materials are shown in Fig. 2. The results of the SPP measurements are provided in Table 2. Note that since the smallest SPPs are discernible in ATEM but not in SEM, the mean SPP size determined by ATEM and SEM are not directly comparable (see material *A* in Table 2).

The detailed SPP size distributions are shown in Figs. 3 and 4. The SEM and ATEM results of the SPP size distribution of material *A* (with the smallest SPPs) have been superimposed, since the ATEM analysis are able to resolve the smallest SPPs while this technique often misses the largest SPPs. To make the superposition, the ratio between the SPP area fractions found by SEM and TEM (see Table 2), respectively, was used to correct the ATEM results. Previous investigations of materials with similar heat treatments and chemistry have shown that type *B* and *C* materials do not contain significant number of SPPs smaller than 30 nm [14], which is the SEM cut-off limit in this work. The results of SPP chemical composition analysis of about 40 SPPs of different sizes from each material type are provided in Table 3. From Figs. 3 and 4 and Tables 2 and 3, it is obvious that material *C* contains by far the largest SPPs and the lowest SPP frequency, i.e. the lowest number of SPPs per unit area. Materials *A* and *B* are similar regarding the SPP size distribution of SPPs with diameters ranging from 50 to 175 nm. Material *A,* however, contains a large fraction of SPPs with a diameter smaller than 50 nm, that is missing in both type *B* and *C* materials. The SPP chemical composition is also different for material *A* compared to that of materials *B* and *C.* The Fe/Cr and Fe/Ni ratios in the chromium and nickel bearing SPPs, respectively, are much smaller in material *A* than in materials *B* and *C*, see Table 3.

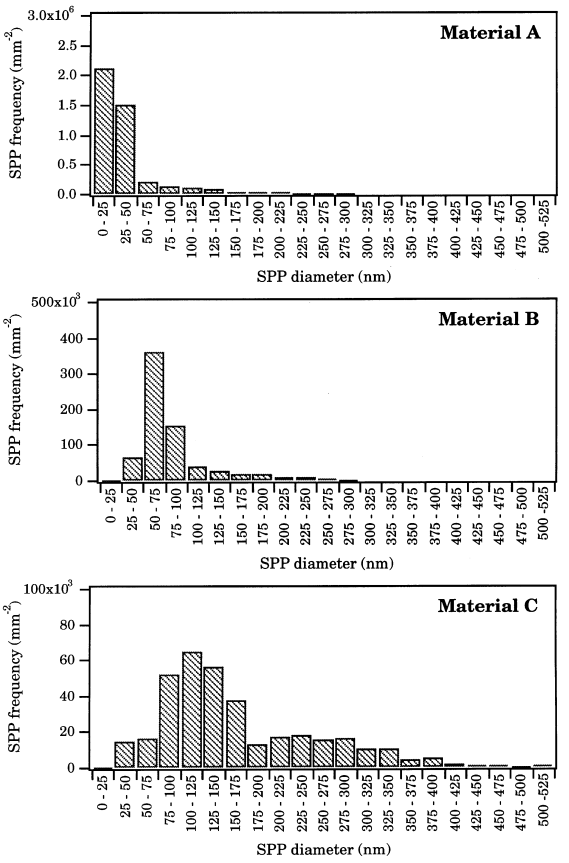

Fig. 3. Histograms of the SPP size distributions for the un-irradiated materials.

3.2.3. Microstructure and SPP distribution of the irradiated materials

A segmented fuel rod with fuel cladding of materials *A, B* and *C,* was irradiated in a Swedish BWR. The

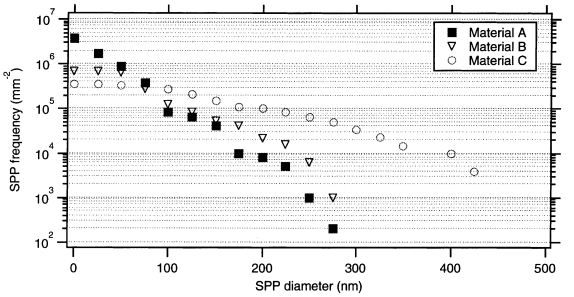

Fig. 4. Cumulative SPP size distribution for the un-irradiated materials. For each of the materials, the graph shows the cumulative number of particles found larger than the SPP diameter given on the *x*-axis.

Table 3
Summary of SPP chemical composition analysis

Material	Instrument (magnification)	Fe/Ni ratio for Fe–Ni SPPs	Fe/Cr ratio for Fe–Cr SPPs
A	ATEM (200 kx)	0.7–0.8	0.4–0.7
B	ATEM (200 kx)	0.9–1.0	0.6–1.1
C	ATEM (200 kx)	0.9–1.0	0.7–1.2

materials were irradiated to a rod average burn-up of 35 MWd/kgU and a fast fluence of 6×10^{25} n/m^2 (E>1 MeV) [15]. Photographs of the three segments are shown in Fig. 5. Transversal cross sections of the different materials are provided in Figs. 6–8.

Material *C* was completely covered by an about 20 μm thick fairly even oxide layer, as shown in Fig. 8. It could be inferred that this material has been subject to a uniform type of corrosion. Visual examinations at lower burn-ups, however, had shown that the material was covered by nodules. Thus, it appears that the nodules have coalesced to such an extent that the oxide layer looks uniform at the higher burn-ups. Figs. 5 and 6 show that the type *A* material has a few nodules, a condition more marked in the plenum region. However, the nodule density on material *A* was much smaller than that of material *B* and at lower burn-up no nodules were visible on material *A*.

The hot cell results are summarised in Table 4 [15]. The oxide thickness of material *C* is about four times larger than that of materials *A* and *B* but the hydrogen content of material *C* is only twice that of the latter materials. Consequently, the integral hydrogen pick-up fraction in material *C* is about half of that in materials *A* and *B*.

Investigation of the SPP distribution by SEM determination of the irradiated samples were also performed and the results are shown in Figs. 9 and 10. Fig. 9 shows clearly that material *A* has lost all the SPPs while the SPPs in materials *B* and *C* still remain. The chemical composition of the matrix was also analysed. The matrix chromium and iron concentrations of material *A* was clearly above the background noise level in the ATEM determinations and corresponded to up to about 700 and 1200 ppm (by weight), respectively. In materials *B* and *C*, the concentration of Fe and Cr in the matrix was not larger than the background noise level.

4. Discussion

4.1. Effect of irradiation on SPPs

The fact that SPPs are important for good uniform corrosion resistance was observed by Blanchet et al. They observed large differences in the corrosion rate of very pure (electron beam-refined crystal-bar) zirconium and Kroll zirconium containing about 1200 ppm of Fe [16]. The pure metal in cold-rolled condition corroded much more rapidly than the Kroll zirconium in 400°C steam and 360°C water. These autoclave tests are used by the industry to predict the uniform corrosion properties of a zirconium material. It was shown in Section 3.2.1 that the solubility of iron, nickel, and chromium in the matrix is about 60–70 ppm in Zircaloy-2. Pure crystal-bar zirconium has very little impurities, and thus contain no or very few SPPs. Kroll zirconium with 1200 ppm of iron had, on the other hand, far more iron than is soluble in the zirconium matrix. Consequently, the Kroll material should have a large number of SPPs. Based upon the results it is indicated that the existence of SPPs in zirconium improves the uniform corrosion resistance.

Not only the presence but also the size distribution and chemistry of the SPPs will be of importance. The corrosion results presented above show that material *C* was more susceptible to nodule formation than material *A* early in-life. There was no significant difference in the iron, chromium, and nickel contents in the material *A, B,* and *C* matrices. However, materials *A* and *C* had large differences in their SPP size distributions, as seen in Figs. 3 and 4. In this case, as in other cases reported [17–23], it can be implied that the alloying elements Fe, Ni, and Cr are important in controlling the corrosion behaviour of the materials. The results show that the matrix composition is rather similar, but not the distribution and chemical composition of the SPPs. We hence infer that the SPPs are important for the development of nodular corrosion.

Since the initial corrosion rate of material *A* was considerably lower than that of material *B,* the corrosion rate at the higher burn-up of the former material must be much larger since the oxide thickness was about equal for the two types of materials in the post-irradiation examination, see Fig. 1. We propose as explanation for this corrosion rate acceleration the dissolution of the SPPs in the *A* material. Such influence on corrosion of irradiation induced SPP dissolution has been reported previously, e.g. [24].

The SPP distribution changes due to irradiation for both materials *B* and *C* where the smallest SPPs dissolve markedly compared to the larger SPPs, Figs. 10 and 11. The data indicate that the larger SPPs actually may grow in size due to irradiation, although this cannot be accurately induced from the limited number of large

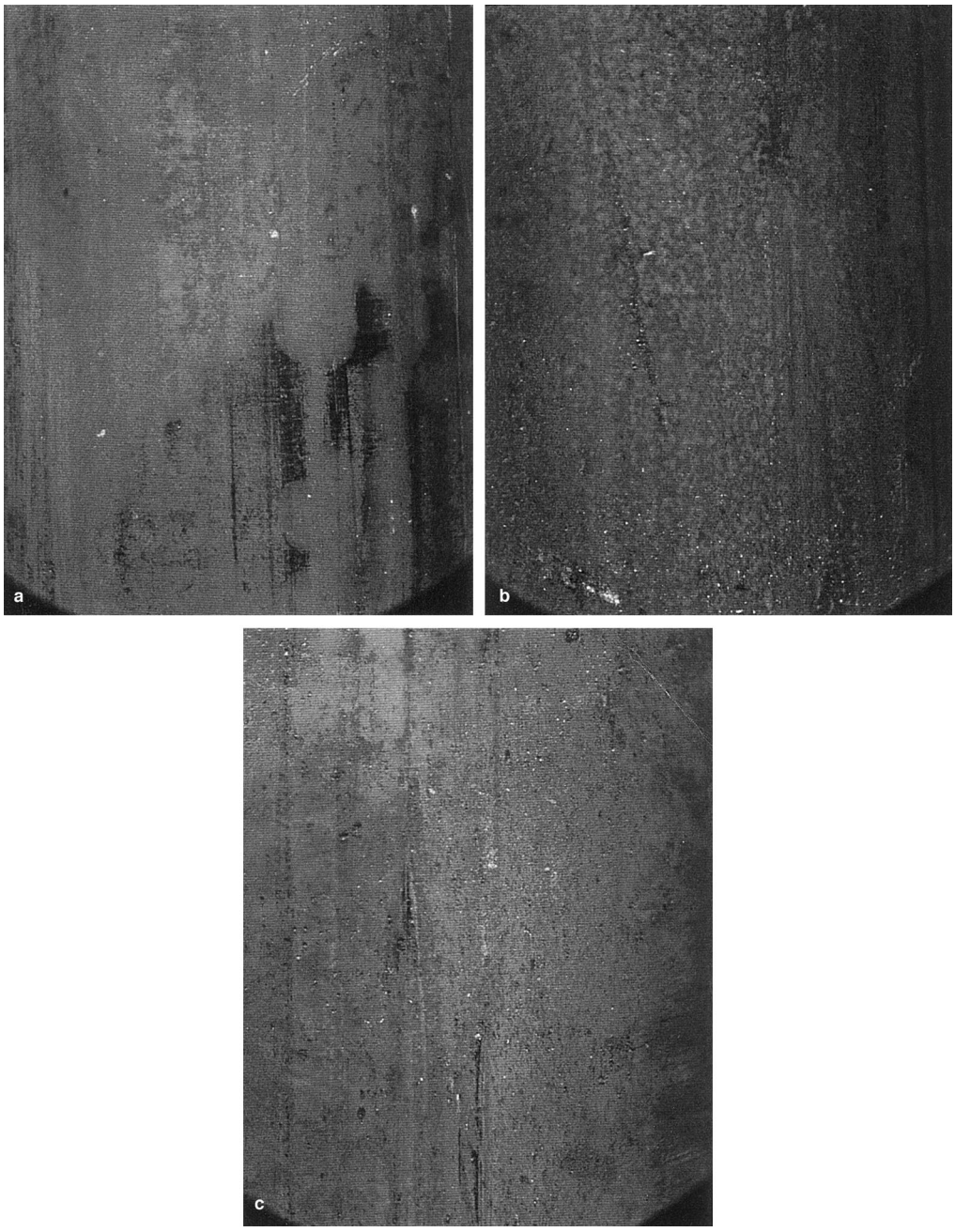

Fig. 5. Photographs of fuel claddings of different materials taken in the hot cell [15], (a) material *A*, (b) material *B*, (c) material *C*.

particles detected in the materials *B* and C in both unirradiated and irradiated conditions.

Material *A*, with the initially smallest SPPs, had lost all of its SPPs during irradiation, as shown by Fig. 9. It is, however, contradicting that the SPPs initially larger than 100 nm in diameter are lost in material *A* while SPPs initially larger than 100 nm are still found in the materials *B* and *C*. The probable explanation to this apparent contradiction is a difference in the SPP stability coupled to the lower Fe/Cr and Fe/Ni ratios in the chromium and nickel bearing SPPs in material *A*, Table 3.

The observations that preferentially smaller SPPs tend to dissolve in the matrix during irradiation and that this dissolution may accelerate the corrosion process has been confirmed in a recent communication [25], where

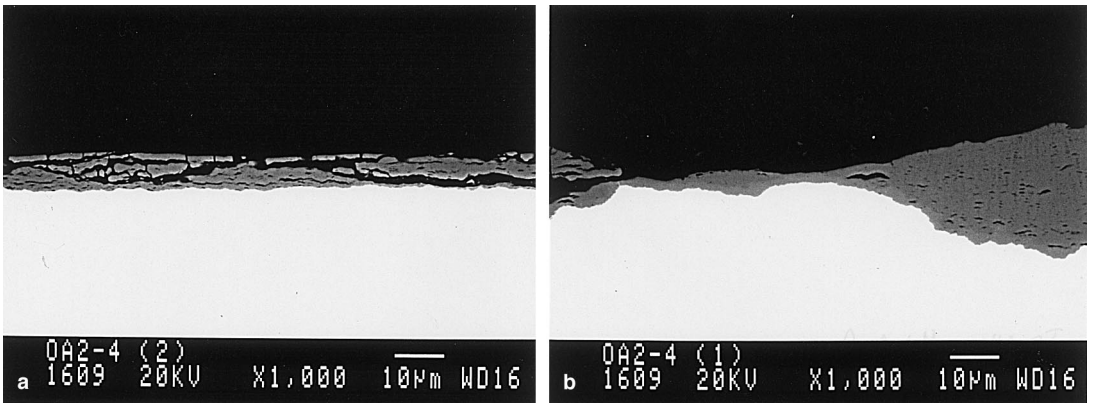

Fig. 6. Typical transversal section of material *A* [15].

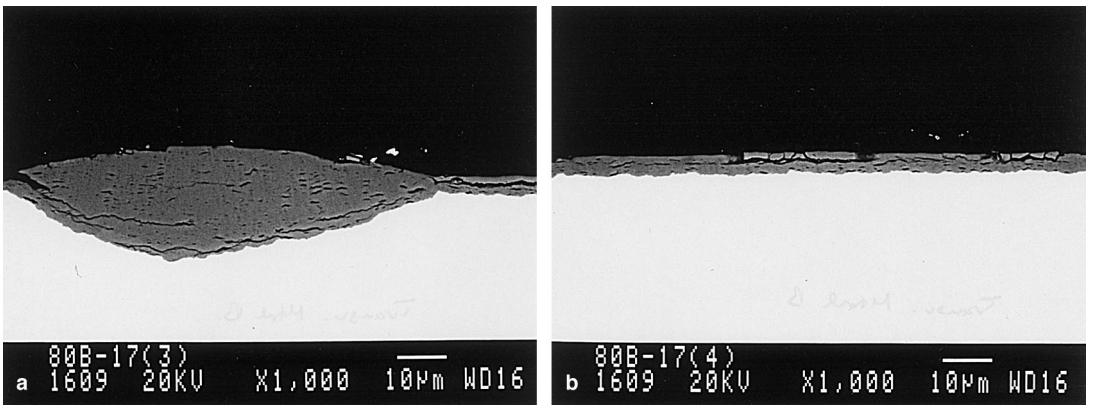

Fig. 7. Typical transversal section of material *B* [15].

Zircaloy-2 coupons were reported to have been manufactured in three different ways, resulting in large differences in the SPP size distributions. The coupons were irradiated in a commercial BWR to fluences between 1.3×10^{25} and 8.5×10^{25} n/m^2 (E >1 MeV). Nodular corrosion was not reported to be observed for any of the materials. At the lowest fluence level, the oxide thickness and hydrogen pick-up fraction was similar in the three materials, approximately 3 μm and 2%, respectively. At the largest fluence level, the number densities of SPPs had decreased in all materials, the smaller the initial SPP size, the larger the decrease. In fact, the SPPs could not be distinguished in the material with the initially smallest SPPs. The resulting oxide thickness, at this fluence, of the material with the initially smallest SPPs was approximately 20 μm while the corresponding value for the material with the initially largest SPPs was about 7 μm. The integral hydrogen pick-up fraction was about 30% for both materials.

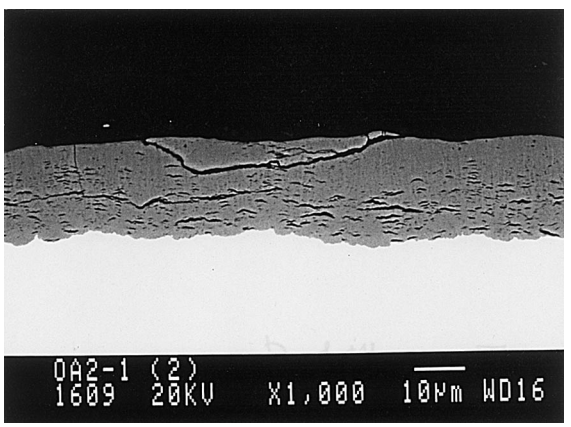

Fig. 8. Typical transversal section of material *C* [15].

A similar observation has been reported by Garzarolli et al. who found a correlation between the BWR corrosion performance of Zircaloy-2 and the material SPP mean size [26]. The results showed that an initial small SPP average size resulted in initially good uniform corrosion behaviours but that late in-life the corrosion

Table 4
Hot cell results of irradiated materials determined by SEM [15]

Material	Hydrogen content (ppm by weight)	Mean cladding outside oxide thickness (μm)
A	94	7
B	96	5
C	203	20

rate was accelerated. If the SPP mean value was too large, the material would experience nodular corrosion resulting in large oxide thicknesses early in-life. Hence, just as in our case, the results indicate that the mean SPP size has to be within a rather narrow range to result in good uniform and nodular corrosion resistance.

4.2. Effect of hydride formation

Hydrides have been shown to affect corrosion behaviour [27–30]. The mechanism behind an increased hydriding accompanied by a corrosion acceleration has, however, not been satisfactorily described.

Zircaloy-4 strip material with an initial hydrogen content of about 20 ppm was steam autoclave tested at 500°C for 24 h [31]. The sample became covered by oxide nodules and the resulting average hydrogen content in the Zr-4 material ranged 1000–4000 wtppm. After this test the nodular oxide was removed on one of the surfaces through grinding, and subsequently subjected to an additional 500°C/24 h steam test. After this second test, the surface with the primary oxide removed now showed a thick uniform oxide. This indicates that nodular oxide may only form if hydrides are precipitated at high local concentration during the corrosion process. If hydrides exists prior to the corrosion test, only uniform oxide may form. Prior to the first test the hydrogen content in the Zr-4 material was below the solubility limit but during the corrosion process large amounts of hydrides were produced locally in the Zr-4 material. In the second test, the hydrogen content was above the solubility limit during the whole test, i.e. there was always large amounts of precipitated hydrides in the material during the corrosion test. The solubility of hydrogen in Zircaloy at 500°C is about 500 ppm by weight [32].

Some additional information on the impact of hydrides on the corrosion process was also found in another 500°C/24 h test [31] of a Zr-4 strip material. The material exhibited different degrees of corrosion acceleration for material surfaces with radically different textures. The texture influenced the orientation of the hydrides, produced during the corrosion reaction, as the hydrides preferentially precipitated in the zirconium basal plane [33]. A second 500°C/24 h test with the primary oxide mechanically removed on all surfaces, showed that the uniform oxide formed in this second test grew faster into the exposed hydrides than into the Zr-matrix.

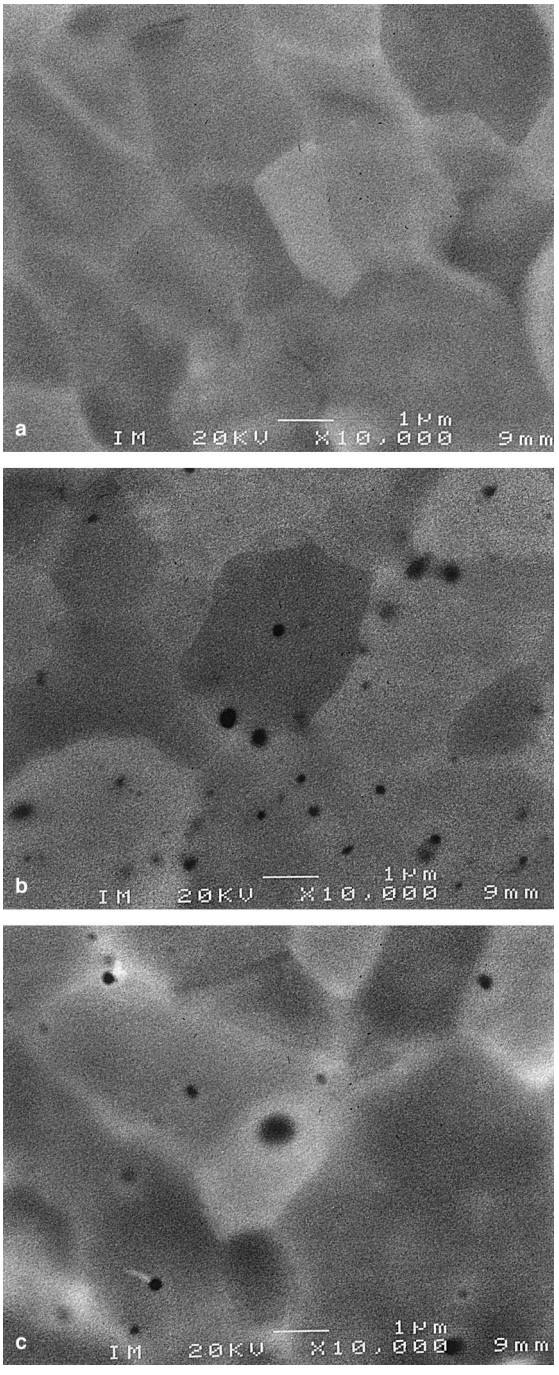

Fig. 9. Micro-graphs of the three irradiated cladding materials (at approximately 35 MWd/kg fuel burn-up), (a) material *A*, (b) material *B*, (c) material *C*, all 10 000× magnification in ASEM in BSE mode.

Blat et al. reported [27] that uniform corrosion acceleration in the 400°C steam test after 60 days of exposure occurred for samples that had been pre-hydrided

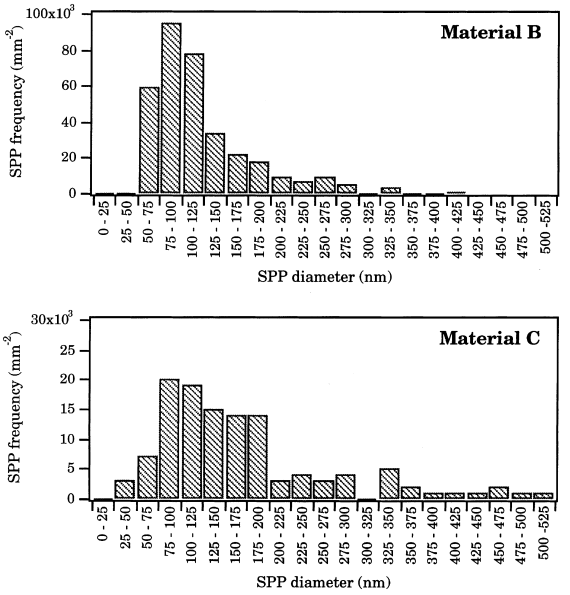

Fig. 10. Histograms showing the SPP size distributions of the irradiated materials (in the irradiated material *A* no SPPs were discernible).

to levels higher than 250 ppm of hydrogen, a level that well agrees with the solubility limit of hydrogen at 400°C [32]. A more elevated hydrogen content was found to corresponded to a higher corrosion rate. Again, this shows that precipitated hydrides present during these corrosion tests accelerates the uniform corrosion rate. It was moreover shown by Blat et al. that cathodic charging results in a more pronounced acceleration compared to that of gaseous charging producing similar average levels of absorbed hydrogen. This is explained by the fact that the hydrides formed by cathodic charging are more superficial, i.e. the local hydride concentration at the corrosion front by the metal/oxide interface is much higher in this case. A very interesting observation was also that the initial hydrogen content did not impact the pre-transition corrosion rate (within a three-days test). This implies that the rate limiting step of corrosion is different during the pre-transition phase to that during the post-transition corrosion, since the hydrogen content affects the latter process but not the former.

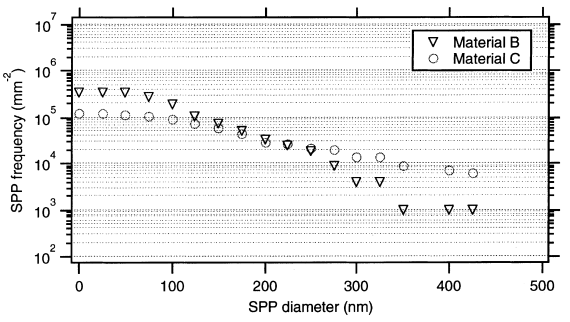

Fig. 11. Cumulative SPP size distribution of the irradiated materials.

Hydrides have also been shown to accelerate uniform corrosion in PWRs [30]. Due to a pellet–pellet gap a cold zone was formed resulting in a locally elevated hydride concentration in this region. The oxide thickness was much larger at the pellet–pellet gap compared to the pellet mid-face, despite the fact that the cladding temperature was considerably lower at the pellet–pellet gap region due to the absence of heat flux. In a PWR reactor, a temperature decrease of 15°C normally results in a drop in corrosion rate of a factor of two for in other aspects similar conditions, e.g. [34]. This proves again that hydrides do accelerate the corrosion process notably.

Based on these facts, we note that hydrides increase the corrosion rate in autoclaves and in-pile. This acceleration is dependent on the hydride concentration in the zone affected by the corrosion process and could be most pronounced. We further propose that this process is the governing process for nodular corrosion. Zirconium hydrides are then precipitated locally during the corrosion reaction. The locally precipitated hydrides will in turn accelerate the corrosion process, explaining the auto-catalytic appearance of the nodular corrosion phenomenon.

We further note that the influence of hydrides is not seen in the pre-transition process i.e. the initial cubic growth seen in zirconium alloys when exposed to steam or air. However, hydrides may dramatically impact the post-transition corrosion process. This implies that the rate limiting steps are different in the pre- and post-transition corrosion regions, a conclusion further elaborated in the next section.

5. Theory of BWR nodular and uniform corrosion and hydriding mechanisms

A bi-directional transport of electrical charges (by ions, electrons, or holes) through the oxide layer occurs at an equal rate to balance charge in corrosion reactions when the substrate has a passivating oxide layer. Furthermore, for a series multi-step corrosion reaction that has attained a steady state, the forward net rate of each step that constitutes the overall reaction must be equal. The slowest step, i.e. the step that in the current situation has the lowest net reaction rate, will determine the overall rate, and will hence be the rate-limiting step. For parallel processes, the fastest step will determine the rate and for a mixed series and parallel multi-step process,

the influence of the various steps can be assessed according to these principles.

The oxide on zirconium base alloys with common amounts of alloying elements consists of three layers in oxides thicker than a few micrometers, as has been shown by EIS (electrochemical impedance spectroscopy) and other measurements [35]. The outer layer is rather porous from a charge and matter transport perspective, although the relative volume of the pores still can be very small [35]. The middle layer is moderately porous, but dense enough to form a transport hindrance to some extent. The inner layer is dense and protective and is often called the barrier layer [36]. The water molecule migrates comparably fast through the porous and permeable outer oxide layers and reaches the dense barrier layer. Close to or in the barrier layer, the water molecule dissociates, possibly into an oxygen ion (O^{2-}) and two protons (H^{+}) [37,38] or into some other species. The species containing oxygen and at least some fraction of the hydrogen species is transported towards the metal–oxide interface. Once the oxygen reaches the metal phase, it forms zirconium and tin/niobium oxide or is dissolved in the metal phase. A similar step-wise transportation will affect any hydrogen species originating from the corrosion process and which eventually will form dissolved hydrogen or hydrides in the metal. The transport step(s) could be preceded and succeeded by one or several adsorption, desorption, or diffusion steps. For hydrogen it is also necessary that it involves at least one redox reaction step. The second phase particles, that have been found to be un-oxidised at least one micrometer into the oxide [39], may play an important role in the charge and hydrogen transports.

The overall corrosion reaction is hence in the form of several process steps in series and in parallel. Each of these steps must be a diffusion, migration, adsorption, desorption, redox or phase transition step which can be affected by the local geometry and stress situation. The inhomogeneities of the oxide, metal–oxide interface and the metal, on the microscopic scale makes it at present difficult to identify, separate, and determine each of these steps. Based on empirical observations, we instead distinguish each process step by parameters known to affect the overall process. We are in this context aware that each such corrosion parameter process step may consist of one or several fundamental mechanistic steps (diffusion, migration, etc.), but that the overall rate of these steps can be modelled with one such corrosion parameter process. The overall corrosion rate is in turn controlled by several corrosion parameter process steps.

The important inference from the observations is that there are several corrosion process steps with different reaction rates. The rate of each such corrosion process step will be affected by variation in the alloys chemical composition and manufacturing process but also, for a given material, with the development of the overall corrosion process. For a given material, normally different corrosion processes will be rate controlling during the pre-transition and post-transition stages. Also, there are, normally, different corrosion processes that are rate controlling during subsequent post-transition corrosion phases.

5.1. Model for the oxidation process

The situation with several corrosion processes being operating simultaneously can be illustrated by modelling the overall corrosion process with corrosion process steps linked in parallel and series. In this first tentative model, we use inverse rate constants or reaction 'resistances', designated RR. It is important to note that the reaction resistances are not to be interpreted as electrical resistances as can be determined by impedance spectroscopy, for instance. Each reaction resistance is related to a specific corrosion step, as illustrated in Fig. 12, and will be further discussed below. The important analogy with common electrical resistances is that the series reaction resistance that has the highest value or the shunting parallel reaction resistance having the lowest reaction resistance, i.e. the rate limiting step, will govern the overall corrosion rate.

For Zircaloy corrosion, investigators have suggested that the rate limiting step may be (i) the diffusion rate of oxygen ions through the barrier layer or the electron conduction rate through the SPPs in the zirconium oxide layer [40–45] and (ii) the oxygen diffusion rate into the metal from the oxide at the oxide/metal interface. The rate limiting step of materials transport through the barrier layer is modelled by RR_{SPP} in Figs. 12 and 13. This reaction resistance is related to the barrier layer thickness, a larger thickness would increase the reaction resistance, i.e. decrease the corrosion rate. The barrier layer thickness is related to the SPP size distribution, as discussed below. If the SPPs are dissolved due to irradiation amorphisation, the RR_{SPP} will decrease to a low value, thus accelerating the corrosion process if this reaction step was rate limiting.

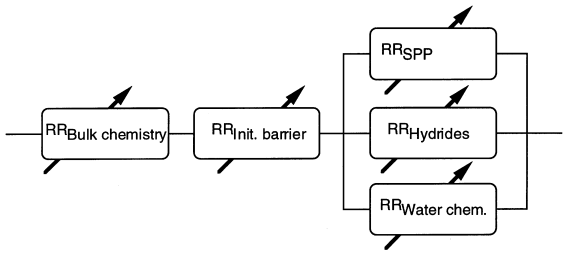

Fig. 12. Schematic picture of the oxidation mechanism.

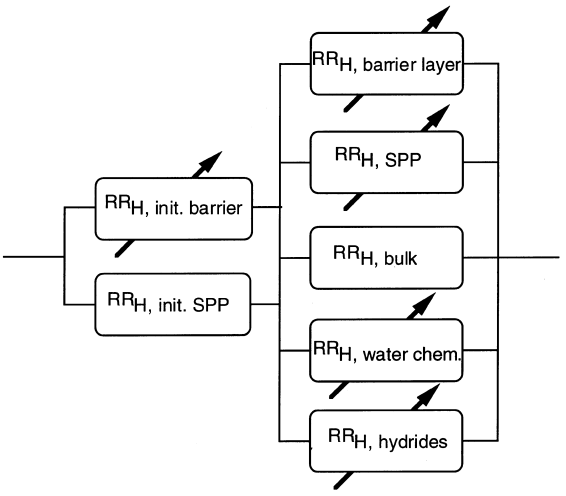

Fig. 13. Schematic picture of the hydriding mechanisms.

It has been reported that decreasing the tin content from 3.3% to 1.5 wt% in Zircaloy-2 variants decreased the BWR corrosion rate significantly [46]. It is proposed that the lattice stresses are smaller between tin and zirconium atoms than between zirconium atoms. Thus, decreasing the tin content from, for example, 3.3% to 1.5 wt% would result in fewer tin-to-zirconium atom bonds, hence the activation energy for oxygen ion diffusion will increase. $RR_{\text{bulk chemistry}}$ is related to the impact of elements such as tin and niobium, dissolved in the zirconium alloy matrix, on the oxygen anion diffusion rate into the matrix. We propose in the following that these elements in solid solution may change the activation energy for oxygen ion diffusion in the metal.

RR_{hydrides} is controlled by the hydrogen content and hydride orientation at the corroding interface. A corrosion acceleration would occur if a sufficient amount of zirconium hydrides are formed at the oxide/metal interface. The RR_{hydrides} would decrease, resulting in a drastic increase in the corrosion rate.

$RR_{\text{water chemistry}}$ accounts for the impact of water chemistry on corrosion, illustrating the less studied and specified influence of water chemistry on Zircaloy corrosion [47].

Tentatively, we propose a model according to Fig. 12, based on the observation that the corrosion rate can accelerate due to influence of barrier layer deterioration, influence of excessive hydride formation, or acceleration due to a aggressive water chemistry, as discussed below. The effective barrier layer reaction resistance will be given by RR_{SPP} in parallel with RR_{hydrides} and $RR_{\text{water chemistry}}$, i.e. $RR_{\text{barrier layer}} = RR_{\text{SPP}}//RR_{\text{hydrides}}//RR_{\text{water chemistry}}$. The $RR_{\text{barrier layer}}$ is initially rate determining in the post-transition stage but often the influence of alloy bulk chemistry seems to be rate determining in long term corrosion, these effects thus operating in series.

5.2. The pre-transition regime

The corrosion process of fuel cladding zirconium alloys is normally showing a cubic oxide growth initially up to an oxide thickness of a few micrometers. This cubic growth seems to be controlled by the oxide film thickness, i.e. a barrier layer, in a similar way for many zirconium alloys despite a large variation in amounts of alloying elements. We therefore propose that this reaction resistance, $RR_{\text{init. barrier}}$, is rate controlling for all alloys, see Fig. 12. The transition into the post-transition region is governed by the break-down of this resistance, probably by mechanical stress or electrical breakdown. This reaction resistance hence will increase by a cubic relation and at a certain thickness will breakdown to very low reaction resistance, leaving other reaction resistances to be controlling. That the initial barrier layer is unique and will not be re-occurring, despite a cyclic behaviour sometimes being reported from autoclave results of Zircaloys, has been shown elsewhere [35].

5.3. Model for the hydrogen up-take mechanism

The hydrogen pick-up is a product of the corrosion rate and the hydrogen pick-up fraction. The water chemistry, such as the oxygen potential, impacts the hydrogen pick-up fraction. It is for instance well-known that the hydrogen pick-up fraction is larger in a PWR than a BWR reactor, probably due to the higher oxidation potential in the BWR case. Thus, increasing the oxidation potential in the coolant will increase the reaction resistance, designated $RR_{\text{H, water chem.}}$ in Fig. 13. It has also been shown that the corrosion rate inherently impacts the hydrogen pick-up fraction [48]. Also in this case the barrier layer thickness is important. The hydrogen atoms may take two routes into the metal, either through the SPPs (at normal barrier layer thicknesses) or directly through the barrier layer. The latter route is only possible when the barrier layer thickness is very small, since the solubility of hydrogen in the zirconia is negligible [36]. The hydrogen transport through the barrier layer is modelled by the reaction resistance of $RR_{\text{H, barrier layer}}$. $RR_{\text{H, SPP}}$ is related to the SPP and will be affected by the size and chemical composition of the SPPs. Nickel containing SPPs are inferred to give a smaller reaction resistance than chromium bearing particles. Less data generally are available on the hydrogen pick-up compared to the oxide thickness for various materials, especially from in-pile conditions. The model of the hydrogen pick-up reaction resistances presented in Fig. 13 is therefore to some extent preliminary.

5.4. Hydriding in the pre-transition regime

We infer that, initially, in the pre-transition regime, the hydrogen pick-up fraction may be large due to the very thin barrier layer. Thus, the value of $RR_{H,\ init.\ barrier}$ is initially very small. The increasing barrier layer thickness during the pre-transition growth dramatically increases the $RR_{H,\ init.\ barrier}$ value. This situation would result in a dramatic decrease in the hydrogen pick-up fraction during the course of oxidation in the pre-transition regime. The situation can however, be less straightforward than in the case of oxidation, since the SPPs could be effective in allowing a large hydrogen transport rate also in the pre-transition stage, a phenomenon that evidently is not the case for the oxygen transport. $RR_{H,\ init.\ barrier}$ is therefore postulated to be in parallel with a second reaction resistance $RR_{H,\ init.\ SPP}$. At present, we however lack accurate experimental data on hydrogen pick-up during the pre-transition corrosion stage to confirm this.

5.5. Nodular corrosion in the post-transition regime

The proposed nodular corrosion mechanism is schematically depicted in Fig. 14. It has been shown that nodules are formed where large SPPs are found, or where agglomerates of smaller SPPs are detected [14]. This circumstance can be explained by the fact that larger SPPs still in metallic contact with the Zircaloy matrix will be able to form a local area for electron transfer, water reduction [49], and hydrogen transport, e.g. [50]. Consequently, a larger local in-flux of hydrogen into the Zircaloy metal will result in the vicinity of larger SPPs. If the influx of hydrogen is larger than the rate of which hydrogen may diffuse away further into the metal, hydrides may form beneath the SPP, as shown in Fig. 14. For material *A* with a relative small number of large SPPs, the influx of hydrogen at each SPP will be lower and seem even to be so low as to be close to or below the maximum rate at which the hydrogen can diffuse away into the bulk alloy. In this case no hydrides will form at the metal/oxide interface and hence no nodules would form in material *A*. Material *B* and *C* had a rather high nodule frequency already early in life during irradiation. Material *A* had no nodules initially. Considering the results presented in Fig. 3, it is hence proposed that the minimum critical SPP size for nodule nucleation is at least 175 nm for in-pile BWR exposure. It is further proposed that there is only a fraction of these SPPs larger than 175 nm that are capable to form nodules. A higher density of SPPs larger than 175 nm will increase the tendency of nodule formation. When the number density of the larger SPPs is sufficiently small, no nodules will form initially, as found for material *A*.

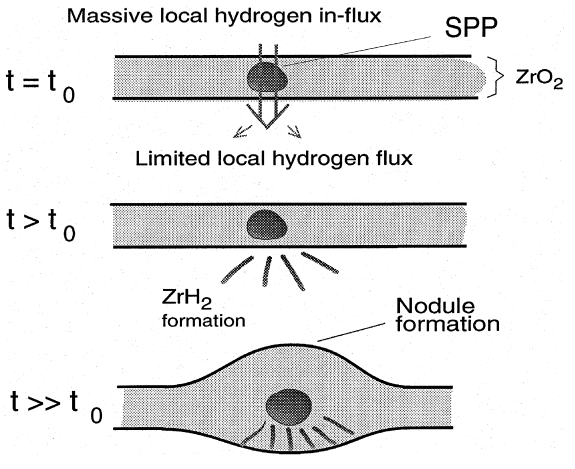

Fig. 14. Schematic nodular corrosion mechanism.

In the following we propose an explanation to the fact that nodular corrosion is found in-pile and in autoclave tests only within a narrow range of conditions. Nodules are normally only found in the temperature range 500–550°C in autoclaves. We propose that it is only in this temperature range that the in-flux of hydrogen, preferentially through the SPPs, is larger than the maximum flux of hydrogen away from the alloy matrix adjacent to the SPPs. Thus, it is only in this temperature range that hydrides will precipitate locally during the corrosion reaction and nodules are formed due to local corrosion acceleration because of the hydride formation. The same outline can explain the differences between the in-pile nodular corrosion behaviour in PWRs and BWRs. The cladding temperature in PWRs are significantly higher (320–400°C) than that in BWRs (280–320°C). The higher temperature increases the hydrogen diffusion rate in Zircaloy and also the solubility in Zircaloy. Consequently, no nodules will normally form in PWRs since the in-flux of hydrogen will be lower than the flux of hydrogen away from the region just below the SPPs, despite the fact that the hydrogen pick-up fraction normally is 20–25% in PWRs but only 5% in BWRs.

For BWRs, as is apparent for materials *B* and *C*, the corrosion rate gets very high at the onset of nodular corrosion. However, this corrosion rate levels off at higher burn-ups due to that the barrier layer that is initially broken down under the influence of nodular corrosion heals. It is suggested that the material is most prone to nodular corrosion initially, when many large SPPs, may bridge the barrier layer thickness when this is small. At a later point the barrier layer thickness, formed by uniform oxide growth, may be larger than the size of the SPPs and at this point the SPPs are not as effective as before to let the hydrogen get access to the Zircaloy material. This means that less hydrides will

form beneath the SPPs that may destroy the barrier layer thickness and therefore the corrosion rate will decrease. Since material *C* has larger SPPs, nodular corrosion may work more actively in this material than in material *B*.

5.6. Uniform corrosion in the post-transition regime

Monoclinic zirconia is the stable phase below about 1200°C [51]. The tetragonal zirconia phase may be stabilised under the influence of large compressive stresses in the oxide [52]. The largest amount of tetragonal zirconia has been found at the oxide/metal interface and decreases towards the outer surface [45]. It has also been found that the tetragonal phase does not form a continuous layer but is irregularly distributed in the oxide [35]. Tetragonal zirconia may arrest propagating cracks through a martensitic phase transformation from tetragonal to monoclinic zirconia [53–56]. Hence, a propagating crack in the monoclinic oxide phase entering a region of tetragonal phase, will relieve the compressive stresses close to the tetragonal phase, below the critical level to maintain the meta-stable tetragonal zirconia. Consequently, the tetragonal phase will undergo a phase transformation to a monoclinic phase with a resulting volume expansion of 7%. This volume expansion will result in a number of very small cracks at the large crack tip due to the fact that the material is brittle. The many small cracks at the propagating crack tip will blunt the crack and the cracking will be stopped.

By use of transversal metallographic examinations of the metal/oxide interface, it was found by Hutchinson and Lehtinen that in between the oxide growing protrusions there exist a region of concavity or cusping [57]. They suggested that the growing oxide would exert a compressive stress on the cusps of metal and that the rate of oxidation at these points would be diminished. The cusps would then tend to drag behind the rest of the growth front. As the residual metal would be oxidised, it would adopt the form of narrow tongues that would be subject to large compressive stresses. Hutchinson and Lehtinen further suggested that the stresses would be large enough to stabilise the tetragonal zirconia as the metal was oxidised and thus produce veins, normal to the metal–oxide interface, of tetragonal zirconia. The veins formed could then act as crack stoppers due to the contents of tetragonal phase, as discussed above. Since the SPPs have a lower affinity to oxygen than does zirconium, the SPPs will oxidise at a slower rate. The surrounding metal will be consumed in the course of oxidation and locations in the vicinity of the SPPs can become compressed to the extent that the tetragonal zirconia phase will be locally stabilised. Hutchinson and Lehtinen suggested however that the SPPs have to be larger than a critical size to disturb the oxidation front to such an extent that tetragonal zirconia could be formed. They proposed also that as the tetragonal phase in a vein becomes farther away from the metal–oxide interface, the relaxation of compressive stresses in the surrounding oxide would decrease below the value at which the tetragonal phase could be stabilised and accordingly the tetragonal phase in the vein would transform into monoclinic oxide. It was suggested that all the veins close to the metal–oxide interface would arrest any propagating crack from the outer oxide regions and it could then be expected that a material with large number of veins in the oxide closest to the metal–oxide interface would have a thicker barrier layer. The barrier layer is hence proposed to be thicker for a higher density of SPPs above the critical size.

For two different arbitrary materials with different volume fraction of SPPs, a thicker barrier layer will be formed in the material with the larger SPP frequency (only considering SPPs larger than the critical size as discussed above) resulting in the lowest post-transition corrosion rate. For two fuel cladding materials with equal alloying composition but different heat treatments in the alpha region, there will be a lower number of SPPs for the material with higher heat input during manufacturing. Veins would form from all SPPs above the critical size. The material with the lowest number of SPPs, i.e. the largest SPPs, would have relatively few veins and the cracks could propagate further down towards the oxide/metal interface resulting in a relatively thin barrier layer. A material with the same volume fraction of SPPs but with much smaller SPPs would instead form a lot of veins, able to arrest propagating cracks. This would hence result in a thicker barrier layer. Consequently, there exists an optimum SPP size, close to the minimum critical size to form a barrier layer, $d_{\min.}$, corresponding to optimum corrosion performance, as illustrated in Fig. 15. With increasing SPP size, still for a given volume fraction of SPPs, the corrosion resistance will decrease.

This reasoning can be used in comparing the BWR corrosion performance of materials *A*, *B* and *C*, as

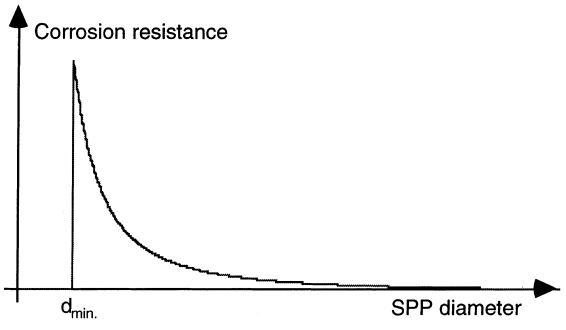

Fig. 15. Schematic influence of SPP size on barrier layer thickness at a constant SPP volume fraction.

shown in Fig. 4. Initially, most of the SPPs in material *A* are larger than the minimum critical SPP size to form a barrier layer and the uniform corrosion and hydrogen pick-up rate will be low. The chemical composition of the SPPs in material *A* was very different from that of materials *B* and *C*. The SPP Fe/Cr ratio in the former material ranged from 0.4 to 0.7 while the corresponding ratio for the latter materials was 0.6 to 1.2, as shown in Table 3. The Fe/Ni ratio is also lower for material *A*, but the difference is smaller for these SPPs.

The SPP will be amorphised under irradiation and iron will preferentially diffuse into the matrix. During the dissolution process, the iron atoms have to diffuse out from the SPP into the matrix and with larger SPPs, the diffusion distance will increase, and hence the diffusion rate will decrease. Larger SPPs will consequently not show the same extent of dissolution as the smaller ones at equal irradiation conditions. It is further proposed that smaller Fe/Cr and Fe/Ni ratios in the chromium- and nickel-bearing SPPs, respectively, make the SPPs less stable during irradiation. Due to the small SPPs and the low Fe/Cr and Fe/Ni ratios in material *A*, the SPPs will dissolve relatively rapidly. The corrosion rate and hydrogen pick-up fraction will increase dramatically as the number of SPPs above the critical size, i.e. large enough to form veins, is coming close to zero. At this stage, the barrier layer thickness is very small, as depicted in Fig. 16. Material *B* with initially somewhat larger SPPs and with SPPs with larger Fe/Cr and Fe/Ni ratios will retain its SPPs to a larger extent even at high burn-ups. For material *C*, the dissolution of SPPs will be much slower than that in material *A* and also material *B* due to its initially larger SPP mean size and the large Fe/Cr and Fe/Ni ratios. The SPPs in materials *B* and *C* are initially much larger than the minimum critical size and hence the barrier layer thickness will not change much during irradiation. The uniform corrosion rate and hydrogen pick-up fraction will consequently be rather constant during the irradiation process for materials *B* and *C*. However, due to the large SPPs in these materials the barrier layer thickness will locally decrease in size early in life due to interaction between the precipitated hydrides and the barrier layer resulting in nodular corrosion, as described in Section 4. The in-pile corrosion data for materials *A*, *B*, and *C* given in Fig. 1 show that material *A* initially has very good uniform corrosion resistance. This implies that material *A* has a significant barrier layer thickness at this stage. From Figs. 3 and 4 it is also obvious that material *A* has a much larger frequency of SPPs larger than 25 nm in diameter compared to materials *B* and *C*. It is inferred from the results that the minimum critical SPP size is below approximately 25 nm.

5.7. Break-away uniform corrosion

The dissolution of the SPPs, as was found for material *A*, proceeds to a complete degradation of the barrier layer thickness with a resulting high corrosion rate and a very high hydrogen pick-up fraction late in-life. The higher corrosion rate will increase the hydrogen concentration close to the metal/oxide interface and hence accelerate the corrosion process further. Hydrogen samples from claddings taken at high burn-ups when the acceleration has begun will give an average of the pick-up during the full residence time in the reactor. This means that even if the hydrogen pick-up fraction at this point could be 100%, the recorded integral pick-up

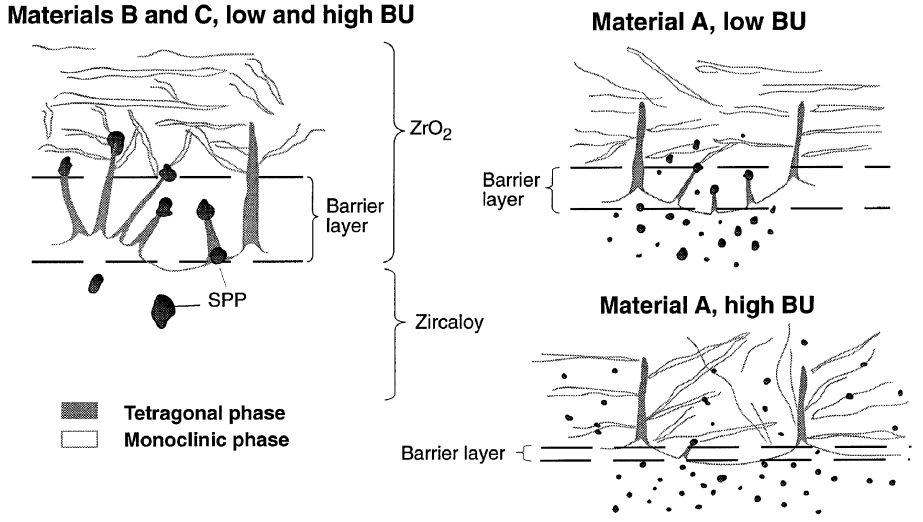

Fig. 16. A schematic view of the effect of SPP dissolution in material *A* as compared to materials *B* and *C* during irradiation and the resulting barrier layer thickness. The formation of tetragonal phase in veins was proposed by Hutchinson and Lehtinen [57].

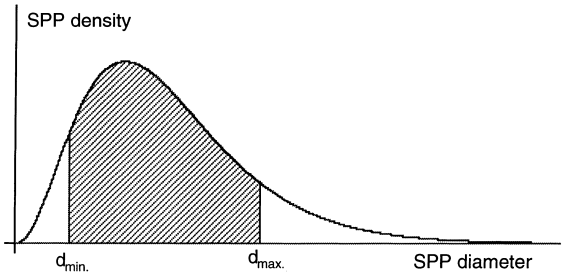

Fig. 17. Hypothetical SPP size distribution to get optimum nodular and uniform corrosion (hatched area).

would be considerably lower due to the lower pick-up fraction early in life.

5.8. SPP size distribution for optimum corrosion and hydriding performance

In Fig. 17, a typical SPP size distribution is plotted for a material. The minimum critical SPP size for barrier layer formation $d_{min.}$ and the maximum critical SPP size for protection against nodular corrosion $d_{max.}$ are also included in the figure. The values of d_{min} and d_{max} depends on corrosion temperature and increase with temperature. Based on the results for BWR materials in this study, a material will have appropriate corrosion and hydriding performance during a full life in a BWR if the SPP size distribution lies between approximately 25 and 175 nm. It is then important that a sufficient number of SPPs are close to d_{min}, since this will produce a thicker barrier layer. The SPPs must, however, be large enough not to be dissolved to a significant degree during the full life irradiation. The composition of the SPPs regarding iron, chromium and nickel, is also important and the conclusions of the SPP size range given in this work is limited to iron-to-nickel ratios between 0.9 and 1.0 and a iron-to-chromium ratio between 0.6 and 1.2, respectively.

Acknowledgements

The work presented here is based on work carried out in a Swedish research programme for the understanding of Zircaloy corrosion and hydriding mechanisms. This programme was funded by ABB Atom and the Swedish utilities Vattenfall AB, OKG, and Barsebäck Kraft AB, which are all gratefully acknowledged. We thank Börje Lehtinen at the Swedish Institute of Metals Research, Stockholm, Sweden, for the investigations of the SPPs and the examination of the nodules formed in autoclave environments. We further acknowledge Hans-Olof Andrén and Boel Wadman at the Chalmers Institute of Technology for performing the atom probe analysis and Tord Jonsson of Studsvik Material AB for the photographs taken at the PIE. Several points brought forward by the reviewer has called for improvement of the paper which we gratefully acknowledge.

References

[1] T. Andersson, T. Thorvaldsson, A. Wilson, A.M. Wardle, Proc. IAEA Int. Symp. on Improvements in the Water Reactor Fuel Technology and Utilisation, Stockholm, 1986, IAEA SM-288/59, IAEA, Vienna, 1987, p. 435.
[2] B. Wadman, H.-O. Andrén, A.-L. Nyström, P. Rudling, H. Pettersson, J. Nucl. Mater. 200 (1993) 207.
[3] P.-A. Elisson, MSc thesis, Chalmers University of Technology, Sweden, 1990.
[4] N.V. Bangaru, R.A. Busch, Proceedings Workshop Second Phase Particles Matrix Prop. Zircaloys, Erlangen, Germany, 1985, p. 101.
[5] D. Pêcheur, F. Lefebvre, A.T. Motta, C. Lemaignan, In: A.M. Garde, E.R. Bradley (Eds.), Proceedings of the 10th International Symposium Zirconium in the Nuclear Industry, Baltimore, MD, ASTM STP 1245, 1994, p. 687.
[6] B. Cheng, Proc. NACE Symp. Environmental Effects on Nucl. React. Mat., Myrtle Beach, SC, NACE, 1983.
[7] M. Griffith, G.J.C. Carpenter, R.W. Gilbert, J. Nucl. Mater. 150 (1987) 53.
[8] D. Pêcheur, F. Lefebvre, A.T. Motta, C. Lemaignan, D. Charquet, J. Nucl. Mater. 205 (1993) 445.
[9] Y. Etoh, S. Shimada, J. Nucl. Sci. Techn. 29 (1992) 358.
[10] Y. Etoh, S. Shimada, J. Nucl. Mater. 200 (1993) 59.
[11] F. Lefebvre, C. Lemaignan, Proc. IAEA Techn. Comm. Mtg. Fundamental Aspects of Corrosion of Zirconium Base Alloys in Water Reactor Environments, Portland, Oregon, 1989, IWGFPT/34, IAEA, Vienna, 1990, p. 80.
[12] M. Griffith, R.W. Gilbert, B.A. Cheadle, Proceedings Workshop Second Phase Particles Matrix Prop. Zircaloys, Erlangen, Germany, 1985, p. 67.
[13] W.J.S. Yang, R.P. Tucker, B. Cheng, R.B. Adamson, Proc. Workshop. Second Phase Particles Matrix Prop. Zircaloys, Erlangen, Germany, 1985, p. 85.
[14] P. Rudling, B. Lehtinen, Mechanistic Understanding of Nodular Corrosion, EPRI Report TR-103396, 1993.
[15] T. Jonsson, S. Bengtsson, STUDSVIK/N(H)-95/02, 1995.
[16] Blanchet et al., J. Nucl. Mater. 22 (1967) 55.
[17] M. Harada, K. Abe, T. Furuya, T. Kakuma, Proc. Workshop. Second Phase Particles Matrix Prop. Zircaloys, Erlangen, Germany, 1985, p. 41.
[18] M. Inagaki, K. Akahori, H. Maki, Proc. Workshop. Second Phase Particles Matrix Prop. Zircaloys, Erlangen, Germany, 1985, p. 123.
[19] K.-Y. Huang, J. Nucl. Mater. 136 (1985) 16.
[20] D. Charquet, J. Nucl. Mater. 160 (1988) 86.
[21] R. Kuwae, K. Sato, E. Higashinakagawa, J. Kawashima, S. Nakamura, J. Nucl. Mater. 119 (1983) 229.
[22] Y. Ito, T. Furuya, J. Sci. Techn. 32 (1995) 1118.
[23] B. Cox, Oxidation of Zirconium and its Alloys, in: M.G. Fontana, R.W. Staehle (Eds.), Advances in Corrosion Science and Technology, vol. 5, Plenum, NY, 1976, p. 73.
[24] R.M. Kruger, R. Adamson, J. Nucl. Mater. 205 (1993) 242.

[25] P.Y. Huang, S.T. Mahmood, R.B. Adamson, in: E.R. Bradley, G.P. Sabol (Eds.), Proc. 11th Int. Symp. Zirconium in the Nucl. Industry, Garmisch-Partenkirchen, Germany, ASTM STP 1295, 1996, pp. 726–755.
[26] F. Garzarolli, R. Schumann, E. Steinberg, 10th Int. Symp. on Zirconium in the Nucl. Industry, ASTM STP 1245, 1994, p. 709.
[27] M. Blat, D. Noel, in: E.R. Bradley, G.P. Sabol (Eds.), Proc. 11th Int. Symp. Zirconium in the Nucl. Industry, Garmisch-Partenkirchen, Germany, ASTM STP 1295, 1996, pp. 319–335.
[28] A. Garde, in: C.M. Eucken, A.M. Garde (Eds.), 9th Int. Symp. Zirconium in the Nucl. Industry, Kobe, Japan, ASTM STP 1132, 1991, p. 566.
[29] T. Kido, 6th Int. Symp. Environment. Degr. Mat. Nucl. Power Systems, San Diego, 1993.
[30] G. Vesterlund, L. Corsetti, Proc. Int. Topical Meeting on Light Water Reactor Fuel Performance, West Palm Beach, ANS, 1994, p. 62.
[31] H. Bergqvist, Studsvik Material AB, unpublished results.
[32] J.J. Kearns, J. Nucl. Mater. 22 (1967) 292.
[33] H. Kawanishi, S. Ishino, Y. Mishima, ASTM STP 551, 1974, p. 201.
[34] B. Cox, ASI Series E: Applied Sciences, vol. 266, Kluwer Academic, Dordrecht, 1994, p. 183.
[35] G. Wikmark, P. Rudling, B. Lehtinen, B. Hutchinson, A. Oscarsson, E. Ahlberg, in: E.R. Bradley, G.P. Sabol (Eds.), Proc. 11th Int. Symp. Zirconium in the Nucl. Industry, 1995, Garmisch-Partenkirchen, Germany, ASTM STP 1295, 1996, pp. 55–72.
[36] IAEA, Corrosion of Zirconium Alloys in Nuclear Power Plants, IAEA-TECDOC-684, IAEA, 1993.
[37] F.W. Trowse, R. Sumerling, A. Garlick, ASTM STP 633, p. 236.
[38] M.F. Sheppard, C. Tyzack, ASTM STP 633, 258.
[39] D. Pêcheur, F. Lefebvre, A.T. Motta, C. Lemaignan, D. Charquet, in: A.M. Garde, E.R. Bradley (Eds.), Proc. 10th Int. Symp. Zirconium in the Nucl. Industry, Baltimore, MD, ASTM STP 1245, 1994, p. 687.
[40] B. Cox, Proc. State Committee Utilisation Atomic Energy of the USSR Conference on Reactor Materials Science, Alushta, USSR, 1978.
[41] N. Ramasubramanian, J. Electrochem. Soc. 127 (1980) 2566.
[42] B.G. Parfenov, V.V. Gerasimov, G.I. Venediktova, Corrosion of Zirconium and Zirconium Alloys, Atomizat, Moscow, 1967, translated from Russian, Israel Program for Scientific Translations, Jerusalem, 1969, p. 50.
[43] H. Stehle, F. Garzarolli, A. Garde, P. Smerd, ASTM STP 824, 1984, p. 483.
[44] F. Garzarolli, H. Sedel, R. Tricot, J.P. Gros, in: C.M. Eucken, A.M. Garde (Eds.), 9th Int. Symp. Zirconium in the Nucl. Industry, Kobe, Japan, ASTM STP 1132, 1991, p. 395.
[45] J. Godlewski, J.P. Gros, M. Lambertin, J.F. Wadier, H. Weidinger, in: C.M. Eucken, A.M. Garde (Eds.), 9th Int. Symp. Zirconium in the Nucl. Industry , Kobe, Japan, ASTM STP 1132, 1991, p. 416.
[46] Y. Etoh, S. Shimada, T. Yasuda, T. Ikeda, R.B. Adamson, J.-S.F. Chen, Y. Ishii, K. Takei, in: E.R. Bradley, G.P. Sabol (Eds.), Proc. 11th Int. Symp. Zirconium in the Nucl. Industry, Garmisch-Partenkirchen, Germany, ASTM STP 1295, 1996, pp. 825–848.
[47] P. Rudling, G. Wikmark, G. Vesterlund, in: Proc. Topical Meeting on Nuclear Fuel, vol. 1, Würzburg, Germany, 1995, p. 264.
[48] D. Charquet, P. Rudling, M. Mikes-Lindbäck, P. Barberis, in: A.M. Garde, E.R. Bradley (Eds.), Proc. 10th Int. Symp. Zirconium in the Nucl. Industry, Baltimore, MD, ASTM STP 1245, 1994, p. 80.
[49] H.G. Weidinger, H. Ruhmann, G. Cheliotis, M. Maguire, T.-L.- Yau, in: C.M. Eucken, A.M. Garde (Eds.), 9th Int. Symp. Zirconium in the Nucl. Industry, Kobe, Japan, ASTM STP 1132, 1990, pp. 499–534.
[50] L. Schlapbach, F. Meli, A. Züttel, Intermetallic Hydrides and their Applications, in: J.H. Westbrook, R.L. Fischer (Eds.), Intermetallic Compounds. Principles and Practice, vol. 2, Wiley, New York, 1995, pp. 475–488.
[51] J.P. Abriata, J. Garces, R. Versaci, in: R.W. Cahn, P. Haasen, E.J. Kramer (Eds.), Material Science and Technology, VCH, New York, 1994, p. 12.
[52] K. Arashi, T. Yagi, S. Akimoto, Y. Kudoh, Phys. Rev. (1990) 4309.
[53] F.F. Lange, J. Mater. Sci. 17 (1982) 225.
[54] D.L. Porter, A.G. Evans, A.H. Heuer, Acta Metall. 27 (1979) 1649.
[55] A.G. Evans, N. Burlingame, M. Drory, W.M. Kiven, Acta Metall. 29 (1981) 447.
[56] A.H. Heuer, M. Rühle, Acta Metall. 33 (1985) 2101.
[57] B. Hutchinson, B. Lehtinen, J. Nucl. Mater. 217 (1994) 243.